INORGANIC CHEMISTRY FRONTIERS

RESEARCH ARTICLE

View Article Online
View Journal | View Issue



Cite this: *Inorg. Chem. Front.*, 2023, **10**, 7212

# Surface functionalization of discrete metal-chalcogenide supertetrahedral clusters and the photocatalytic application†

Jin Wu, [a,b] Qiang Fu,[b] Zixin Wu,[b] Peipei Sun,[a,b] Xing Zhu,[c] Ying Wang,[c] Ning Chen, [b] Dong-Sheng Li [d] and Tao Wu *[a,b]

Received 26th May 2023,
Accepted 15th October 2023

DOI: 10.1039/d3qi00983a

rsc.li/frontiers-inorganic



Atomically precise metal-chalcogenide supertetrahedral clusters (MCSCs) are supposed to be more attractive for functionalization than conventional metal-sulfide quantum dots owing to their potential ability to establish precise structure–composition–property relationships. However, the accurate surface functionalization of such cluster-based species remains difficult. In this paper, we present a facile method for synthesizing discrete MCSCs decorated with different functional groups *via* a one-step solvothermal reaction, which was demonstrated to have better solvent dispersibility compared with ligand-free ones. In addition, the composites were also prepared by combining ligand-free clusters (or ligand-partially protected or amino-modified ones) with two-dimensional MXene nanosheets. The composites derived from amino-modified clusters exhibited optimal performance of photocatalytic hydrogen evolution. Furthermore, the hydrogen bonding interactions between modified amino groups and MXene nanosheets were verified by $^1$H-NMR spectroscopy. This work provides a facile approach for the surface functionalization of MCSCs, and facilitates the expansion of the functionality of atomically precise nano-species.

## Introduction

Discrete metal-chalcogenide supertetrahedral clusters (MCSCs), known as ultra-small "quantum dots", represent regularly fragmented units of zinc blende type materials.[1–6] Since their structures can be accurately identified at the atomic level, they have been widely studied in the fields of fluorescence,[7–13] photocatalysis,[14–20] and electrocatalysis[21–25] for establishing an accurate structure–composition–property relationship. However, such clusters usually exhibit poor dispersibility and conductivity during practical applications, and the weak binding forces between clusters and conductive substrates limit their further development.[26–32] Therefore, rational modification of clusters for improving the interactions between clusters and conductive substrates would be helpful for their applications in catalysis.

Owing to the advancement of organic template-guided synthesis, most of the discrete T*n* and P*n* clusters (two main types of MCSC structures, where *n* represents the number of metal layers in the basic cluster units, Scheme S1†) reported in recent years are predominantly ligand-free types.[29] The high-degree negative charges of these clusters are usually balanced by protonated organic amines (*i.e.*, counterions), which results in poor dispersibility and instability. Alternatively, a group of C*n* clusters (fully coated with organic ligands, Scheme S1†) has superior dispersibility. However, their monomeric composition and poor structural tunability make them a suboptimal choice for subsequent functional applications. Therefore, by combining the advantages of the above two types of structures, a series of ligand-partially protected T*n* and P*n* clusters has been developed (Scheme S2†). The few ligands at the cluster surface help to improve their contact with the solution molecules and reduce their negative charge density, thereby improving structural stability and dispersibility. This feature is well-suited for functional expansion, and makes them a promising choice.

Since MCSCs generally exhibit poor electrical conductivity, combining them with a suitable conductive substrate is desirable for promoting the separation of the photogenerated electrons and holes, which may effectively enhance photo-

[a]*College of Chemistry and Materials Science, Guangdong Provincial Key Laboratory of Functional Supramolecular Coordination Materials and Applications, Jinan University, Guangzhou, 510632, China. E-mail: wutao@jnu.edu.cn*
[b]*College of Chemistry, Chemical Engineering and Materials Science, Soochow University, Suzhou, Jiangsu 215123, China*
[c]*Testing and Analysis Centre, Soochow University, Suzhou, Jiangsu 215123, China*
[d]*College of Materials and Chemical Engineering, Hubei Provincial Collaborative Innovation Centre for New Energy Microgrid, Key Laboratory of Inorganic Nonmetallic Crystalline and Energy Conversion Materials, China Three Gorges University, Yichang 443002, China*

†Electronic supplementary information (ESI) available: Supplementary tables and figures, PXRD patterns, EDS and $^1$H-NMR analysis. CCDC 2254140–2254148 for **ISC-24**, **ISC-25**, **ISC-25-4′-NH$_2$**, **ISC-25-4′-CH$_3$**, **ISC-25-4′-OH**, **ISC-25-4′-F**, **ISC-25-4′-OCH$_3$**, **ISC-26-2′-NH$_2$** and **ISC-26-4′-Cl**. For ESI and crystallographic data in CIF or other electronic format see DOI: https://doi.org/10.1039/d3qi00983a

catalytic performance. In recent decades, MXenes, a layered transition metal carbide/carbonitride/nitride family, have attracted attention in many scientific fields, such as energy storage and conversion,[33] sensing,[34] and photocatalysis.[35–38] In the domain of photocatalytic hydrogen evolution (PHE), $Ti_3C_2T_x$ is one of the most studied MXenes for the following reasons: (1) the favorable hydrophilic ability supports its chemical reactions within aqueous solutions;[39] (2) the excellent electrical conductivity promotes the separation and transfer of the photoinduced charge carriers from semiconductors;[40] and (3) the appropriate work function allows it to form a Schottky heterojunction with most semiconductors. Therefore, the ultra-thin $Ti_3C_2T_x$ substrate is regarded as a suitable and promising substrate, in which abundant surface O/F sites can also serve as potential hydrogen bonding receptors for anchoring discrete MCSCs.

This work aims to improve the interactions between a cluster and a conductive substrate by manipulating the cluster surface environment, and eventually, improve the performance of photocatalytic hydrogen evolution (PHE). On the basis of the synthetic route of P*n*-type clusters that are partially protected by ligands,[32] we changed the types of diphenyl disulfides to modify the cluster surface with different functional groups (Scheme 1). By taking advantage of the large number of O/F sites on the surface of MXene, which can easily form hydrogen bonds with amino-modified clusters, the PHE performance of amino-modified MCSCs (and ligand-free clusters) combined with MXene nanosheets was investigated.

# Experimental

## Materials

All chemicals were purchased from commercial sources and used without further purification. Deionized water was used in all synthetic procedures.

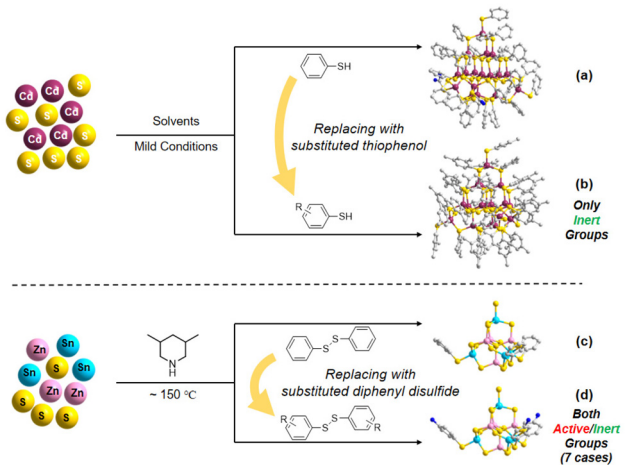


**Scheme 1** Schematics of the surface functionalization of discrete MCSCs: (a and b) using the modified thiophenol and (c and d) using modified diphenyl disulfide.

## Synthetic procedures

**Synthesis of ISC-24, 10(3,5-DMPH$^+$)·[$(Zn_4Sn_4S_{17})^{10-}$]·4$H_2O$.** The synthetic procedure for **ISC-24** followed our previous work,[32] except that the manganese source was replaced by a zinc source. A mixture of zinc acetate tetrahydrate (Zn$(OAc)_2$·4$H_2O$, 120 mg), tin dichloride ($SnCl_2$, 60 mg), sulfur powder (S, 120 mg), 3,5-dimethylpiperidine (3,5-DMP, 3.0 mL), and deionized water ($H_2O$, 1.0 mL) was added to a 25 mL Teflon-lined stainless steel autoclave and stirred for 30 min, then was heated to 125 °C for 7 days. After cooling down to room temperature, transparent colorless block crystals were obtained with a yield of 19.4% based on zinc acetate dihydrate.

**Synthesis of ISC-25, 7(3,5-DMPH$^+$)·[$Zn_4Sn_4S_{14}(SPh)_3^{7-}$]·$H_2O$.** The synthetic procedure for **ISC-25** followed our previous work,[32] except that the manganese source was replaced by a zinc source. Zinc acetate tetrahydrate (Zn$(OAc)_2$·4$H_2O$, 120 mg), tin dichloride ($SnCl_2$, 60 mg), sulfur powder (S, 120 mg), diphenyl disulfide ($Ph_2S_2$, 160 mg), 3,5-dimethylpiperidine (3,5-DMP, 3.0 mL), and deionized water ($H_2O$, 1.0 mL) were mixed in a 25 mL Teflon-lined stainless steel autoclave and stirred for 30 min, then heated to 125 °C for 14 days. After cooling down to room temperature, transparent colorless rhombohedral crystals were obtained with a yield of 16.8% based on zinc acetate dihydrate.

**Synthesis of ISC-25-4′-$NH_2$, 7(3,5-DMPH$^+$)·{[$Zn_4Sn_4S_{14}(SPhNH_2)_3$]$^{7-}$}·$H_2O$.** A mixture of zinc acetate tetrahydrate (Zn$(OAc)_2$·4$H_2O$, 120 mg), tin dichloride ($SnCl_2$, 60 mg), sulfur powder (S, 120 mg), di-(4,4′-amino)-diphenyl disulfide ($S_2(NH_2Ph)_2$, 160 mg), and deionized water ($H_2O$, 1.0 mL) was added to a 25 mL Teflon-lined stainless steel autoclave and stirred for 30 min, then heated to 125 °C for 14 days. After cooling down to room temperature, oblique octahedral or hexagonal transparent crystals were obtained with a yield of 12.6% based on zinc acetate dihydrate.

**Synthesis of other ISC-25 and ISC-26 series samples with different decorated functional groups.** Similar to the synthetic processes described above, the ligand of $Ph_2S_2$ was replaced by substituted $Ph_2S_2$ (*e.g.* $(ClPh)_2S_2$, the categories are summarized in Table S2†) in the same molar ratio with the other components unchanged.

**Preparation of $Ti_3C_2T_x$ nanosheets.** $Ti_3C_2T_x$ nanosheets (here T represents the oxygen terminus generated by HF etching) were synthesized according to the reported method (Schemes S2 and S3†).[41] $Ti_3AlC_2$ powders (>98 wt% purity; particle size <75 μm, *i.e.*, 200 mesh) were immersed in HF (10 wt%) solution at 300 K by stirring for 24 h. Then the resulting suspension was washed several times with deionized water and centrifuged to remove the remaining impurities and HF until the pH value of the solution reached 5–6. The wet sediment was washed twice with ethanol and transferred to a wide-necked jar to air-dry for 3–4 days. The finally obtained sample was named $Ti_3C_2T_x$. The multilayered $Ti_3C_2T_x$ was then stirred with dimethyl sulfoxide (DMSO) at 310 K for 24 h. The colloidal suspension was centrifuged to obtain the intercalated

powders. The powders were then washed several times with deionized water to remove the residual DMSO. Next, the residue was dispersed in deionized water in a weight ratio of $Ti_3C_2T_x$ to water of 1 : 100. Afterward, ultrasonication treatment was carried out for 4 h to exfoliate the $Ti_3C_2T_x$ powder into 2-D sheets under argon. The suspension was centrifuged at 3500 rpm for 10 min to remove the unexfoliated MXenes. Finally, the $Ti_3C_2T_x$ nanosheets were obtained by filtration and dried in a vacuum for further experiments.

**Preparation of P1-CNPs (CNPs: cluster-derived nanoparticles).** **P1-CNPs** were prepared in the mixed solution of formamide and water (1 : 1 in volume). The corresponding crystals of 10 mg of **ISC-24**, **ISC-25**, and **ISC-25-4′-NH$_2$** were ground into powder and dispersed in 10 mL of 1 : 1 formamide/water. After 30 min of ultrasonication treatment, the formamide/water solution of **P1-CNPs** with a concentration of 1 mg mL$^{-1}$ was prepared by mechanical stirring for 4 h.

**Preparation of CMn samples.** **CM*n*** samples were prepared by mixing 1 mg mL$^{-1}$ of the corresponding **P1-CNP** formamide aqueous solution with the one containing the ultra-thin $Ti_3C_2T_x$ nanosheets according to the mass percentage (**CM0** is **P1-CNPs** without $Ti_3C_2T_x$ nanosheets).

## Results and discussion

### Synthetic procedure and crystal structure description

The title compounds constructed from supertetrahedral P1-ZnSnS clusters were obtained by a facile one-step solvothermal reaction (see the Experimental section and the ESI† for details). To directly realize the functionalization of the partially protected P1-ZnSnS, various diphenyl disulfides decorated with different functional groups were selected, and the synthetic routine and molecular structure of the relevant compounds are shown in Fig. 1.

The obtained clusters mentioned in this work are all composed of the $[Zn_4Sn_4S_{17}]^{10-}$ core, so the functionalized samples are represented in a simplified form (*e.g.*, **ISC-25-ZnSnS-SPh** is simplified to **ISC-25**, and the functionalized **ISC-25** are represented as the site of the substituent on their benzene ligand, *e.g.*, **ISC-25-4′-NH$_2$**). The derivatives of **ISC-26** are also showcased in a similar pattern. The structural difference between **ISC-25** and **ISC-26** is the number of protecting ligands (three-corner protected in **ISC-25** and four-corner protected in **ISC-26**, Fig. 1).

Interestingly, **ISC-26-2′-NH$_2$** was obtained using 2,2′-dinitrodiphenyl disulfide, instead of 2,2′-diaminodiphenyl disulfide. This may be attributed to excess sulfur powder in the reaction system, which reduces the nitro group to the amino group. A similar situation also occurs in **ISC-25-4′-NH$_2$**, while **ISC-25-4′-NH$_2$** can also be obtained by directly using 4,4-diaminodiphenyl disulfide. This process is also shown in detail in Table S2.†

A series of functionalized crystalline **ISC-25** and **ISC-26** samples was obtained in the transparent rhombohedral form, but **ISC-26-4′-Cl** appeared in the form of a transparent decagonal octahedron. Single crystal X-ray structural analysis revealed that the **ISC-24** sample crystallized in $P\bar{4}3n$ (No. 218), all **ISC-25** series samples and **ISC-26-2′-NH$_2$** crystallized in the $R\bar{3}$ space group (No. 148), and the **ISC-26-4′-Cl** sample crystallized in the $C2/c$ space group (No. 15). These functionalized clusters are

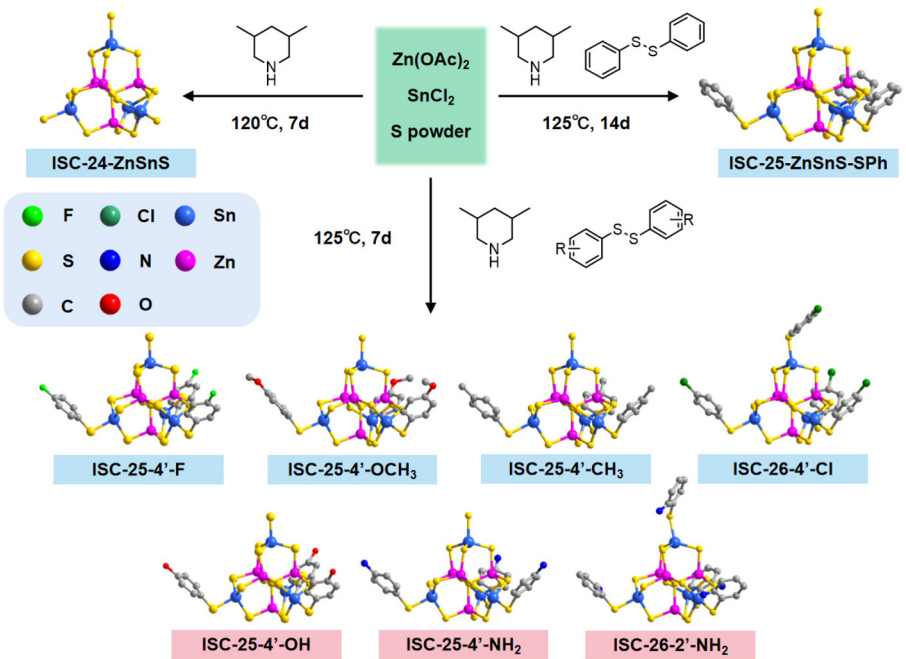


**Fig. 1** Synthetic processes and molecular structures of **ISC-24**, **ISC-25**, and **ISC-25&26** with different functional groups. The products with functional groups have been distinguished by different colored backgrounds in comment boxes (light blue: inert functional groups, *e.g.*, –$CH_3$, –$OCH_3$, –Cl, –F; pink: active functional groups: *e.g.*, –OH, –$NH_2$).

 

basically isomorphic to the structures previously reported.[32] Combined with the results of C, H, and N elemental analysis of **ISC-24**, **ISC-25**, and **ISC-25-4′-NH$_2$** (Table S3†) and their SCXRD data (Table S1†), the formulas of the above three compounds were determined as follows: **ISC-24**: 10(3,5-DMPH$^+$)·[(Zn$_4$Sn$_4$S$_{17}$)$^{10-}$]·H$_2$O; **ISC-25**: 7(3,5-DMPH$^+$)·{[Zn$_4$Sn$_4$S$_{14}$(SPh)$_3$]$^{7-}$}·H$_2$O and **ISC-25-4′-NH$_2$**: 7(3,5-DMPH$^+$)·{[Zn$_4$Sn$_4$S$_{14}$(SPhNH$_2$)$_3$]$^{7-}$}·H$_2$O. Compared to the P1 cluster reported previously, the cluster reported here retained the pristine atomic arrangement of the divalent and tetravalent metal ions, *i.e.*, each P1-ZnSnS contained one $(M^{II}_4S)^{6+}$ and four $(M^{IV}S_4)^{4-}$ units to meet Pauling's electrostatic valence rule.

### Morphology of $Ti_3C_2T_x$ nanosheets and dispersed P1-CNPs

Layered $Ti_3C_2T_x$ nanosheets were prepared by exfoliating bulk $Ti_3AlC_2$ powders in HF aqueous solution. The corresponding structure information for $Ti_3AlC_2$ and the preparation process are shown in Schemes S3 and S4.† After immersing them in HF solution for 24 h, the $Ti_3AlC_2$ powders (200 mesh) were successfully expanded and converted to the layered $Ti_3C_2T_x$ structure (Fig. 2a). The emergence of layers was caused by the fact that the Al layers in $Ti_3AlC_2$ nanoparticles were etched away, and the interlayer space was increased by released $H_2$. After intercalation by dimethyl sulfoxide (DMSO), the layered structures were further delaminated into 2D $Ti_3C_2T_x$ nanosheets by ultrasonication (Fig. 2b). The AFM image in Fig. 2c shows that the thickness of $Ti_3C_2T_x$ nanosheets is about 4 nm. In addition, PXRD characterization was performed on the $Ti_3AlC_2$ MAX phase and $Ti_3C_2T_x$ nanosheets to distinguish the outcome of Al etching. As shown in Fig. 2d, there are a number of characteristic peaks at $2\theta$ = 9.95°, 19.50°, 34.38°, 37.49°, 39.21°, 42.13°, 48.72°, and 56.66°, which correspond to the (002), (004), (101), (103), (104), (105), (107), and (109) planes of the $Ti_3AlC_2$ MAX phase. This result is in agreement with the one in the published literature.[42,43] The degree of the (002) plane in PXRD is generally used to calculate the interlayer spacing of the layered material by applying Bragg's law, and the *d*-spacing of the $Ti_3AlC_2$ MAX phase is calculated to be approximately 5.0 Å. $Ti_3C_2T_x$ MXene nanosheets show a (002) peak at $2\theta$ = 7.42°, referring to a *d*-spacing of 13.6 Å (Fig. 2d). It is clearly demonstrated that the Al layer in the $Ti_3AlC_2$ MAX phase has been well etched, which allows water molecules to further exfoliate the Al layer for preparing single-layered $Ti_3C_2T_x$ MXene nanosheets.[45]

The nanoparticles generated from the cluster dispersion are denoted as **P1-CNPs** (CNPs: cluster-derived nanoparticles) in this work. Three examples of clusters were selected for comparison to test their dispersibility: **ISC-24** without ligand protection, **ISC-25** with a partially protected ligand, and **ISC-25-4′-NH$_2$** with a partially protected ligand modified with amino (–NH$_2$) groups. The corresponding **P1-CNP** solutions were prepared by adding the ground crystals of the above three compounds to the formamide/water solution (1 : 1), followed by stirring for 4 h and sonicating for 1 h. The particle sizes of **P1-CNPs** formed from **ISC-24** were found to be 25–55 nm (Fig. 3a, mean size ~40 nm), which far exceeded the size of individual clusters (~1.6 nm). This suggests that the dispersed particles existed in the aggregated form of multi-clusters. In contrast, the mean particle sizes of **P1-CNPs** formed by ligand-partially protected **ISC-25** and amino-modified **ISC-25-4′-NH$_2$** were found to be 4–7 nm and 1–4 nm, respectively (Fig. 3b and c). The latter two were significantly more accessible to solution. This can be explained by the low negative charge of the clusters and the improved solubility.

In addition, no effective lattice striations were observed in the HRTEM images of the **P1-CNPs** formed by the dispersed clusters. This suggests that **P1-CNPs** have adopted an amorphous state, which is probably due to the small size of the individual clusters (~1.6 nm).

### Fabrication and morphology of P1-CNPs/$Ti_3C_2T_x$ nanocomposites (CM*n*)

The nanocomposites consisting of **P1-CNPs** and exfoliated $Ti_3C_2T_x$ are denoted as **CM*n*** (***n*** indicates the weight percentage of the added $Ti_3C_2T_x$, ***n*** = 0 indicates that no $Ti_3C_2T_x$ was added). The fabrication process for the composite is shown in Scheme S4.† The results of PXRD characterization of **CM1** (composed of **ISC-25-4′-NH$_2$** derived **CM0** and $Ti_3C_2T_x$) are shown in Fig. S11.†

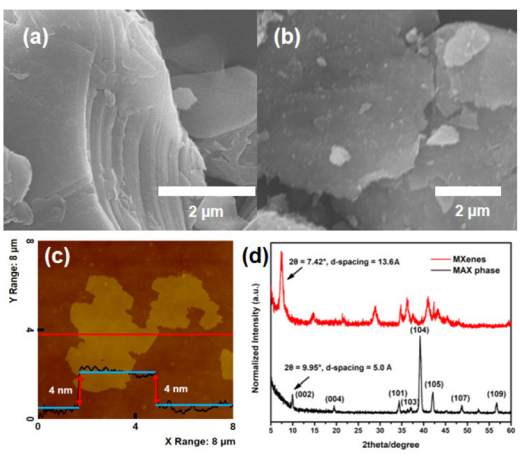


**Fig. 2** SEM images of layered (a) and exfoliated $Ti_3C_2T_x$ nanosheets (b) obtained by HF treatment of $Ti_3AlC_2$ powder; (c) AFM images of dispersed single-layered $Ti_3C_2T_x$ nanosheets; and (d) PXRD results of $Ti_3AlC_2$ powder and exfoliated $Ti_3C_2T_x$ nanosheets.

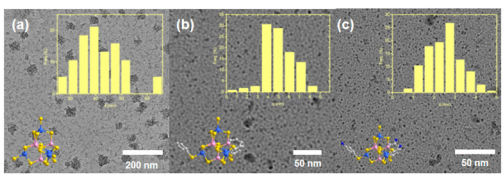


**Fig. 3** TEM images of **P1-CNPs** formed by (a) **ISC-24**; (b) **ISC-25**, and (c) **ISC-25-4′-NH$_2$**, and the insets show the size distribution and the molecular structures of the corresponding clusters.

Due to the low loading amount and low crystallinity, only the diffraction peaks of MXene nanosheets were observed. In order to characterize the morphology and structure of **CM*n***, we performed HRTEM tests on the corresponding samples. Firstly, the morphology of $Ti_3C_2T_x$ was characterized, and clear lattice stripes were observed as shown in Fig. 4a and b. However, for **CM1**, the lattice stripes were not detected in the HRTEM images (Fig. 4c and d). This was also confirmed by the selected area electron diffraction (SAED) characterization. As shown in Fig. S3a,† single-crystal diffraction patterns of $Ti_3C_2T_x$ were observed when selected electron diffraction was performed on the regions shown in Fig. 4a and b, while the **CM1** composites exhibited a polycrystalline form (Fig. S3b†), consistent with the states shown in Fig. 4c and d. In addition, we also performed HAADF-STEM characterization on **CM1** prepared with **ISC-25-4′-NH$_2$** as the precursor, and performed EDS mapping tests (Fig. 4e–j). The constituents of Zn, Sn, S, and N in the clusters were uniformly distributed on the $Ti_3C_2T_x$ nanosheets, demonstrating the successful preparation of the composites.

### PHE performance of CMn

The photocatalytic performance of the above composites was tested by conducting PHE reactions under full-spectrum irradiation using the $Na_2S/Na_2SO_3$ reagent as the sacrificial reagent. Firstly, **ISC-25-4′-NH$_2$** derived **CM0** was selected for the PHE reaction, and the $H_2$ production rate was calculated to be 17.51 μmol $g^{-1}$ $h^{-1}$ according to the data shown in Fig. 5a. This poor PHE performance could be attributed to the low separation efficiency of the photogenerated electron–hole pairs of **CM0**. Enhanced photocatalytic activities were obtained for the **ISC-25-4′-NH$_2$** derived samples containing a certain percentage of $Ti_3C_2T_x$ (1%, 2.5%, 5%, and 10%, *i.e.*, **CM1**, **CM2.5**, **CM5**, and **CM10**, respectively). The PHE rate from **CM1** was calculated to be 158.32 μmol $g^{-1}$ $h^{-1}$ (Fig. 5a and b). This result indicates that the $Ti_3C_2T_x$ nanosheets play an important role in separating the photogenerated electron–hole pairs for **P1-CNPs**. The PHE activity of **CM2.5**, **CM5** and **CM10** decreased to 113.37, 121.07, and 89.43 μmol $g^{-1}$ $h^{-1}$, respectively. These results were caused by the aggregation of $Ti_3C_2T_x$ and **P1-CNPs**, which was verified by its TEM images (Fig. S4†). Under such situation, the $Ti_3C_2T_x$ nanosheets partially mask the active sites of **P1-CNPs**, thereby leading to a reduced photocatalytic efficiency.

The photocatalytic stability of **ISC-24**, **ISC-25**, and **ISC-25-4′-NH$_2$** derived **CM1** composites was also investigated (Fig. 5d–f). The activity of the **ISC-24** derived **CM1** decreased by 52.9% for the second round of photocatalysis, and further decreased by 25.4% to 8.71 μmol $g^{-1}$ $h^{-1}$ in the third round of testing (Fig. 5d). This can be attributed to the poor stability of the **ISC-24** derived sample. For the **CM1** composites prepared with **ISC-25** and **ISC-25-4′-NH$_2$** as precursors, the photocatalytic activity of the second and third rounds decreased by 83.2%, 75.4% and 96.3%, 91.3%, respectively, compared to the first round. The results show that the composites containing **P1-CNPs** with the amino-modified clusters have good stability.

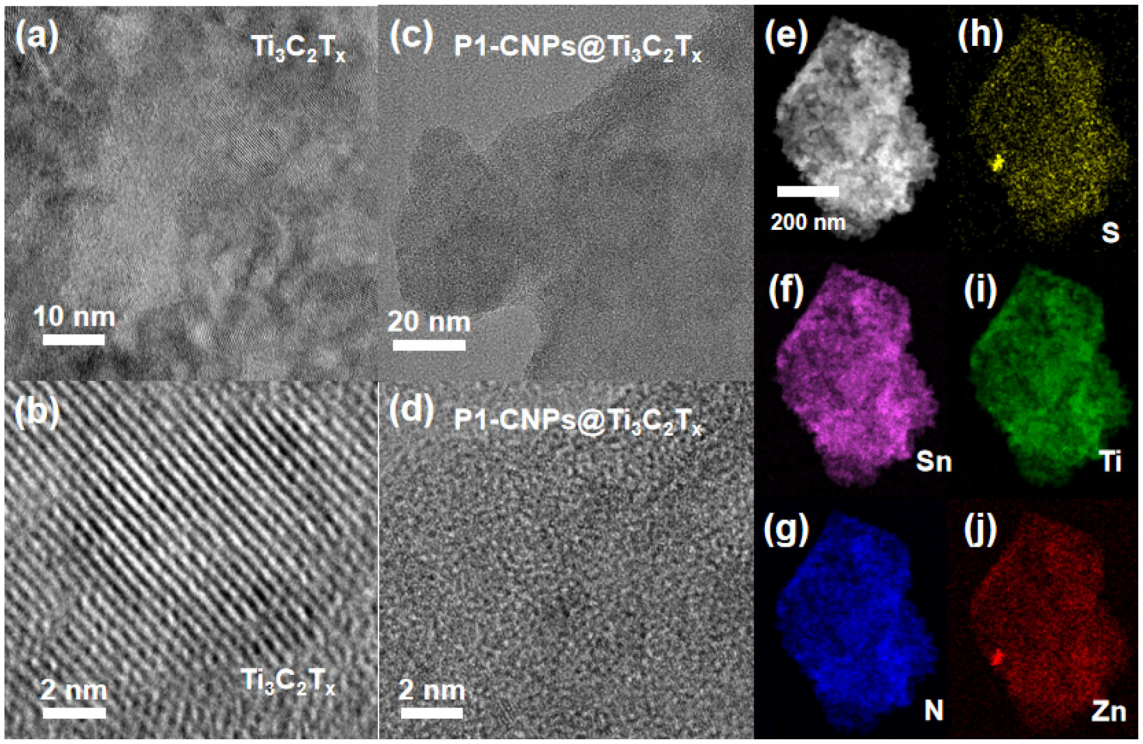


**Fig. 4** HRTEM images of MXene nanosheets (a and b) and **ISC-25-4′-NH$_2$** derived **CM1** (c and d). HAADF-STEM image of P1-CNPs/$Ti_3C_2T_x$ nanocomposites (e), and EDS elemental mapping images of (f) Sn, (g) N, (h) S, (i) Ti, and (j) Zn, respectively.

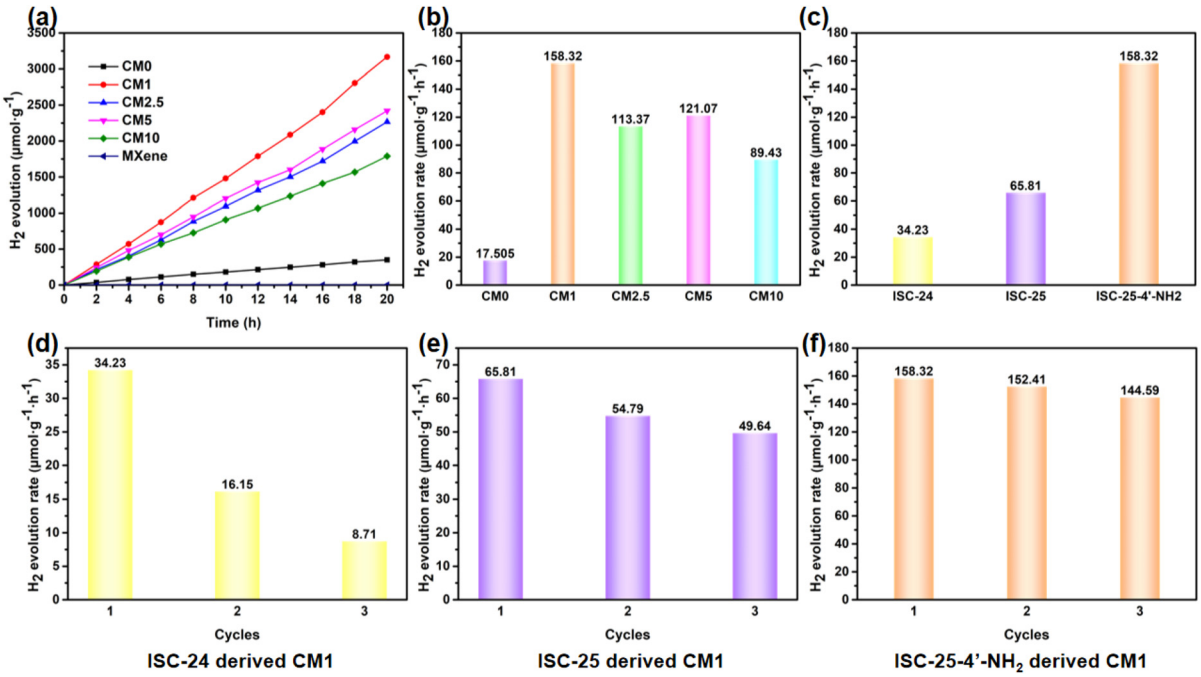


**Fig. 5** Investigation of photocatalytic properties of **CM*n***. (a and b) Comparison of PHE performance of **CM0**, **CM1**, **CM2.5**, **CM5**, and **CM10** nanocomposites under irradiation using **ISC-25-4′-NH$_2$** derived **CM*n***. (c) Comparison of PHE performance of **CM1** composite materials using **ISC-24**, **ISC-25**, and **ISC-25-4′-NH$_2$** derived **CM*n***. (d–f) Test results of multiple cycles on **CM1** composite materials using **ISC-24**, **ISC-25**, and **ISC-25-4′-NH$_2$** derived **CM*n***.

### $^1$H-NMR test for P1-CNPs and CMn

Considering that the **CM1** derived from **ISC-25-4′-NH$_2$** has good PHE performance and high stability, we assume that the amino groups in the modified P1 cluster play an important role. Therefore, the $^1$H-NMR test was conducted to verify the above conjecture (Fig. 6). The formation of hydrogen bonds between the amino groups and the oxygen terminus of $Ti_3C_2T_x$ nanosheets caused the chemical shift values of hydrogen atoms to be shifted towards the lower field due to this effect. Similar situations have been reported in the case of an S···H–N hydrogen bond.[44] In addition, protonated 3,5-dimethylpiperidine, which acts as counterion during cluster dispersion, also interacts electrostatically with the oxygen terminus on the $Ti_3C_2T_x$ nanosheets to form hydrogen bonds, as evidenced by the result of the $H_d$ signal moving from 7.1 ppm to 8.0 ppm in Fig. 6. This interaction also provides a theoretical basis for the enhanced photocatalytic performance of **ISC-24** and **ISC-25** based **CM1** (Fig. 5c).

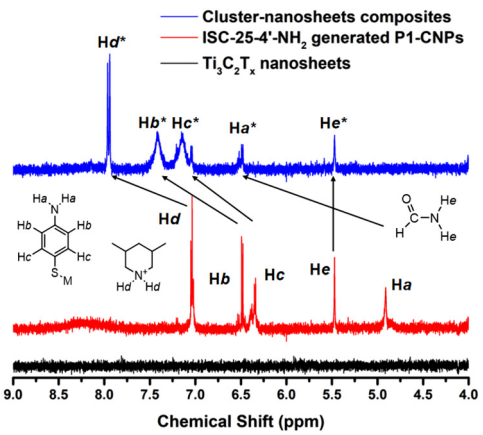


**Fig. 6** $^1$H-NMR spectra of $Ti_3C_2T_x$ nanosheets, **P1-CNPs** formed by **ISC-25-4′-NH$_2$**, and their composite materials with a chemical shift value of 4.0–9.0 ppm (see Fig. S5–S7† for original data).

### Optical and electrochemical properties of CMn

To further understand the enhanced photocatalytic performance of **CM*n*** composites compared to **P1-CNPs**, a series of optical and electrochemical properties were characterized. Firstly, UV–vis absorption spectra were obtained to characterize the light absorption capability of the samples. As shown in Fig. 7a, the light absorption of **CM1** was significantly increased compared to **CM0** in the whole range of 260–460 nm due to the dispersed $Ti_3C_2T_x$ nanosheets, and similar phenomena were observed for **CM2.5**, **CM5** and **CM10**. Subsequently, steady-state photoluminescence (PL) spectra were recorded for the **ISC-25-4′-NH$_2$** derived **CM0** and **CM1**, as shown in Fig. 7b. The emission intensity of **CM1** was significantly weakened compared to that of **CM0**, suggesting that the electron–hole recombination in **CM1** composites is well-suppressed because of the effective charge transfer between **P1-CNPs** and $Ti_3C_2T_x$.

In addition, the photoelectric response and electrochemical impedance spectra (EIS) were recorded to detect the separation of photogenerated electron–hole pairs and the interfacial

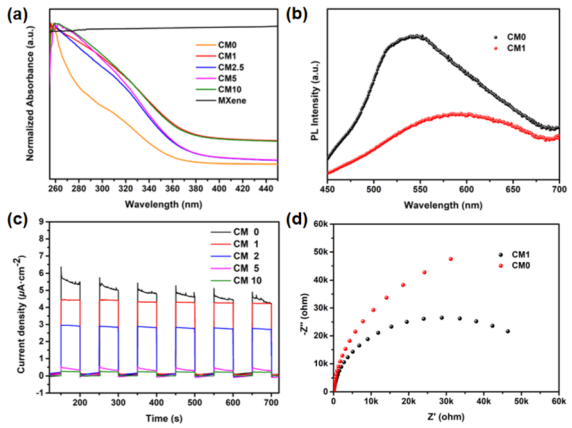


Fig. 7 (a) UV–vis absorption spectra of MXene nanosheets and **CM*n***; (b) PL spectra of **ISC-25-4′-NH$_2$** derived **P1-CNPs** and **CM1** (Ex = 380 nm); (c and d) photoelectric response curves (c) and electrochemical impedance spectra (d) of **ISC-25-4′-NH$_2$** derived **CM*n***.

charge transfer. As shown in Fig. 7c, **CM0** showed the highest transient photocurrent densities, but were less stable compared to the prepared **CM*n*** decorated electrodes. According to this situation, **CM0** should have a higher PHE efficiency. However, considering the feature of sharp reduction of the photocurrent (Fig. 7c), we also compared the EIS curves of **CM0** and **CM1**, as shown in Fig. 7d. The fitted EIS spectra of **CM1** showed a smaller semicircle and a lower interfacial resistance, revealing the more efficient electron–hole pair separation and transfer efficiency of the **CM1** heterostructure. We therefore attribute the low photocatalytic efficiency of **CM0** to poor stability and weak conductivity. **CM1** exhibited the highest photocurrent density in the **CM*n*** series, corresponding to its highest PHE performance and stability, while **CM2.5**, **CM5**, and **CM10** exhibited lower photocurrent densities due to the formation of a sandwich-like structure, as shown in Fig. S4,† where the multilayered $Ti_3C_2T_x$ nanosheets may cover the active sites of **P1-CNPs**.

X-ray photoelectron spectroscopy (XPS) tests were also carried out on **ISC-25-4′-NH$_2$** derived **P1-CNPs**, $Ti_3C_2T_x$ nanosheets, and **CM1** composites to further verify the formation of composites between the two substances, and the results are shown in Fig. S8–S10.† The Zn, Sn and S signals of **ISC-25-4′-NH$_2$** are consistent with those of **P1-CNPs**, and the high-resolution XPS spectra of Ti 2p showed four deconvoluted peaks (Fig. S10†) with binding energies of 464.8 eV and 459.0 eV corresponding to Ti–O $2p^{1/2}$ and Ti–O $2p^{3/2}$ and 461.2 eV and 455.3 eV corresponding to Ti–C $2p^{1/2}$ and Ti–C $2p^{3/2}$, respectively. This result is in agreement with the HRTEM ones described above.

### Photocatalytic mechanism and the band structure

To further understand the enhanced photocatalytic performance of the **CM*n*** series composites compared to **CM0**, we conducted a series of characterization studies. The Mott–Schottky analysis was first performed to evaluate the flat-band potential and Fermi levels of **CM0** and **CM1** prepared from **ISC-25-4′-NH$_2$**.[45–47] As shown in Fig. 8a, the flat-band potentials of **CM0** and **CM1** were calculated to be −0.87 V and −0.26 V (*versus* NHE, pH = 7), which were directly treated as Fermi levels since the surface Fermi levels are very close to the flat-band potential.[48,49] To further determine the valence band (VB) and $E_g$[50] of **CM0** and **CM1**, XPS valence band spectroscopy (VB-XPS) and solid-state UV–vis diffuse reflectance spectroscopy were also carried out. From the VB-XPS results (Fig. 8c and d), the VB positions of **CM0** and **CM1** were determined to be 1.44 eV and 0.96 eV relative to the Fermi level,[51] which indicates that the VB positions of **CM0** and **CM1** are 0.57 V and 0.70 V (*versus* NHE, pH = 7), respectively. The band gaps of **CM0** and **CM1** were found to be 3.27 eV and 3.26 eV, respectively, according to Fig. 8b. The corresponding conduction bands (CB) edges of **CM0** and **CM1** were calculated to be −2.70 V and −2.56 V (*versus* NHE, pH = 7), respectively, by combining the CB = $E_g$ − VB equation.[52]

Based on the above analysis, we proposed a photocatalytic mechanism for illustrating the higher PHE performance of the **CM*n*** series composites, as shown in Fig. 9. After **P1-CNPs** combined with the $Ti_3C_2T_x$ nanosheets to form a binary complex, the Fermi level of **CM1** shifted upwards relative to **CM0**. The Mott–Schottky curve in Fig. 8a shows that **P1-CNPs** are n-type semiconductors and their flat-band potential is much more negative than that of the $Ti_3C_2T_x$ nanosheets, so the close contact between the two components in **CM1** results in the transfer of electrons from the **P1-CNPs** to the $Ti_3C_2T_x$ nanosheets. This is evidenced by the flat-band potential correction (−0.10 V *vs.* NHE) in **CM1** compared to **CM0**, suggesting that the Fermi level of **P1-CNPs** in **CM1** decreases upon their binding to $Ti_3C_2T_x$. A similar situation was reported in the studies of Jakob[53] and Ran.[46] Furthermore, the immobilized positive charges in the **P1-CNPs** are near the **P1-CNPs**/

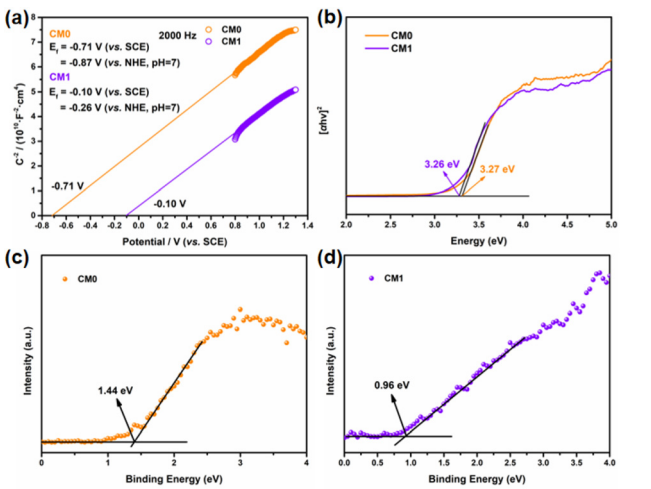


Fig. 8 (a) Mott–Schottky plots of **ISC-25-4′-NH$_2$** derived **P1-CNPs** (*i.e.* **CM0**) and **CM1** composites; (b) solid-state UV–vis diffuse reflectance spectra of **CM0** and **CM1**; (c and d) valence band XPS spectra of **CM0** (c) and **CM1** (d).

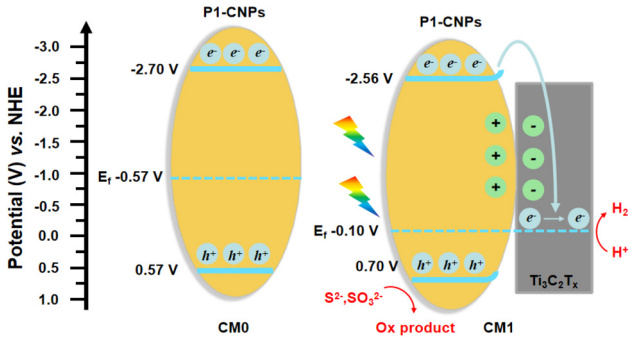


**Fig. 9** Proposed schematic diagram of the photocatalytic mechanism for **CM0** and **CM1** under light irradiation.

$Ti_3C_2T_x$ interface, where a space charge layer (or internal electric field) is formed and the CB and VB in the **P1-CNPs** are bent "upwards", thus forming a Schottky junction between them. Under full-spectrum solar irradiation, electrons are excited from the VB of the **P1-CNPs** to the CB, and due to the reduced thickness of the space charge layer in the **P1-CNP** particles, photogenerated electrons in the CB can still migrate through the "upward" bent CB to the Fermi level of $Ti_3C_2T_x$, leaving photogenerated holes in the VB of **P1-CNPs**. The previously mentioned formation of Schottky junctions can act as electron traps for trapping photogenerated electrons without blocking the transfer of electrons from **P1-CNPs** to $Ti_3C_2T_x$.[54–56] After the transfer of electrons to the $Ti_3C_2T_x$ nanosheets through the above pathway, the excellent electrical conductivity of $Ti_3C_2T_x$ allows electrons to quickly shuttle to the surface. As a result, based on the excellent HER capabilities of $Ti_3C_2T_x$, the **CM*n*** series composites achieved more efficient PHE performance compared to pure **P1-CNPs**.

## Conclusions

In summary, we proposed a strategy for disulfide bond cleavage to prepare discrete MCSCs with multiple active/inactive modified functional groups. Furthermore, three models with different structures were tested for their dispersibility, binding strength with MXene nanosheets, and photocatalytic hydrogen generation performance. The results showed that the amino-modified clusters had better performance than ligand-free type ones. This work provides insights for the subsequent design and synthesis of other types of discrete MCSCs with active functional groups, and is expected to have long-term implications for the functional expansion of metal chalcogenide cluster-based nanomaterials.

## Author contributions

Jin Wu: Investigation, writing – original draft, and writing – review & editing. Qiang Fu and Zixin Wu: TEM image testing. Peipei Sun: data curation. Xing Zhu and Ying Wang: HRTEM and SAED testing. Ning Chen: funding acquisition. Tao Wu: Writing – review & editing, supervision, project administration, and funding acquisition.

## Conflicts of interest

The authors declare no competing financial interests.

## Acknowledgements

The authors acknowledge financial support from the National Natural Science Foundation of China (No. 22071165 and 21875150), and the 111 Project (D20015).

## References

1 J. Zhang, X. Bu, P. Feng and T. Wu, Metal chalcogenide supertetrahedral clusters: Synthetic control over assembly, dispersibility, and their functional applications, *Acc. Chem. Res.*, 2020, **53**, 2261–2272.
2 J. Zhang, P. Feng, X. Bu and T. Wu, Atomically precise metal chalcogenide supertetrahedral clusters: Frameworks to molecules, and structure to function, *Natl. Sci. Rev.*, 2022, **9**, nwab076.
3 S. Santner, J. Heine and S. Dehnen, Synthesis of crystalline chalcogenides in ionic liquids, *Angew. Chem., Int. Ed.*, 2016, **55**, 876–893.
4 B. Peters, N. Lichtenberger, E. Dornsiepen and S. Dehnen, Current advances in tin cluster chemistry, *Chem. Sci.*, 2020, **11**, 16–26.
5 P. Feng, X. Bu and N. Zheng, The interface chemistry between chalcogenide clusters and open framework chalcogenides, *Acc. Chem. Res.*, 2005, **38**, 293–303.
6 Y. Peng, Q. Hu, Y. Liu, J. Li and X. Huang, Discrete supertetrahedral T*n* chalcogenido clusters synthesized in ionic liquids: Crystal structures and photocatalytic activity, *ChemPlusChem*, 2020, **85**, 2487–2498.
7 Z. Wang, Y. Liu, J. Zhang, X. Wang, Z. Wu, J. Wu, N. Chen, D.-S. Li and T. Wu, Unveiling the impurity-modulated photoluminescence from $Mn^{2+}$-containing metal chalcogenide semiconductors via $Fe^{2+}$ doping, *J. Mater. Chem. C*, 2021, **9**, 13680–13686.
8 Y. Liu, J. Zhang, B. Han, X. Wang, Z. Wang, C. Xue, G. Bian, D. Hu, R. Zhou, D. S. Li, Z. Wang, Z. Ouyang, M. Li and T. Wu, New insights into Mn–Mn coupling interaction-directed photoluminescence quenching mechanism in $Mn^{2+}$-doped semiconductors, *J. Am. Chem. Soc.*, 2020, **142**, 6649–6660.
9 T. Wu, Q. Zhang, Y. Hou, L. Wang, C. Mao, S. T. Zheng, X. Bu and P. Feng, Monocopper doping in Cd–In–S supertetrahedral nanocluster via two-step strategy and enhanced photoelectric response, *J. Am. Chem. Soc.*, 2013, **135**, 10250–10253.

10 J. Lin, Q. Zhang, L. Wang, X. Liu, W. Yan, T. Wu, X. Bu and P. Feng, Atomically precise doping of monomanganese ion into coreless supertetrahedral chalcogenide nanocluster inducing unusual red shift in $Mn^{2+}$ emission, *J. Am. Chem. Soc.*, 2014, **136**, 4769–4779.

11 J. Lin, D.-D. Hu, Q. Zhang, D.-S. Li, T. Wu, X. Bu and P. Feng, Improving photoluminescence emission efficiency of nanocluster based materials by in-situ doping synthetic strategy, *J. Phys. Chem. C*, 2016, **120**, 29390–29396.

12 F. Wang, J. Lin, T. Zhao, D. Hu, T. Wu and Y. Liu, Intrinsic "vacancy point defect" induced electrochemiluminescence from coreless supertetrahedral chalcogenide nanocluster, *J. Am. Chem. Soc.*, 2016, **138**, 7718–7724.

13 Q. Zhang, J. Lin, Y.-T. Yang, Z.-Z. Qin, D. Li, S. Wang, Y. Liu, X. Zou, Y.-B. Wu and T. Wu, Exploring $Mn^{2+}$-location-dependent red emission from (Mn/Zn)–Ga–Sn–S supertetrahedral nanoclusters with relatively precise dopant positions, *J. Mater. Chem. C*, 2016, **4**, 10435–10444.

14 N. Zheng, X. Bu, H. Vu and P. Feng, Open-framework chalcogenides as visible-light photocatalysts for hydrogen generation from water, *Angew. Chem., Int. Ed.*, 2005, **44**, 5299–5303.

15 D. Liu, Y. Liu, P. Huang, C. Zhu, Z. Kang, J. Shu, M. Chen, X. Zhu, J. Guo, L. Zhuge, X. Bu, P. Feng and T. Wu, Highly tunable heterojunctions from multimetallic sulfide nanoparticles and silver nanowires, *Angew. Chem., Int. Ed.*, 2018, **57**, 5374–5378.

16 R. Hu, X. L. Wang, J. Zhang, D. Hu, J. Wu, R. Zhou, L. Li, M. Li, D. S. Li and T. Wu, Multi-metal nanocluster assisted Cu–Ga–Sn tri-doping for enhanced photoelectrochemical water splitting of $BiVO_4$ film, *Adv. Mater. Interfaces*, 2020, **7**, 2000016.

17 Z. Wu, X.-L. Wang, X. Wang, X. Xu, D.-S. Li and T. Wu, 0D/2D heterostructure constructed by ultra-small chalcogenide-cluster aggregated quaternary sulfides and g-$C_3N_4$ for enhanced photocatalytic $H_2$ evolution, *Chem. Eng. J.*, 2021, **426**, 131216.

18 W. Yang, X.-L. Wang, N. Kong, C. Liu, P. Sun, Z. Wang, Y. Ding, H. Lin, D. Li and T. Wu, Minimized external electric field on asymmetric monolayer maximizes charge separation for photocatalysis, *Appl. Catal., B*, 2021, **295**, 120266.

19 W. Yang, X. Wang, Z. Wang, P. Sun, J. Tang, J. Li, D.-S. Li and T. Wu, Interstitially O-doped $Cd_xZn_{1-x}S$ solid solution derived from chalcogenide molecular clusters for photocatalytic hydrogen evolution, *Inorg. Chem. Front.*, 2022, **9**, 3771–3778.

20 C. Xue, J. Zhang, X. Wang, M. Gu, Y. Zhu, D. S. Li, J. Guo, Y. Liu and T. Wu, Light-triggered evolution of molecular clusters toward sub-nanoscale heterojunctions with high interface density, *Chem. Commun.*, 2019, **55**, 8146–8149.

21 Y. Zhang, X. Wang, D. Hu, C. Xue, W. Wang, H. Yang, D. Li and T. Wu, Monodisperse ultrasmall manganese-doped multimetallic oxysulfide nanoparticles as highly efficient oxygen reduction electrocatalyst, *ACS Appl. Mater. Interfaces*, 2018, **10**, 13413–13424.

22 D. L. Liu, X. Fan, X. Wang, D. D. Hu, C. Z. Xue, Y. Liu, Y. Wang, X. Zhu, J. Guo, H. P. Lin, Y. Y. Li, J. Zhong, D. S. Li, X. H. Bu, P. Y. Feng and T. Wu, Cooperativity by multi-metals confined in supertetrahedral sulfide nanoclusters to enhance electrocatalytic hydrogen evolution, *Chem. Mater.*, 2019, **31**, 553–559.

23 X. Wang, X.-L. Wang, J. Lv, Z. Wu, J. Zhang, D. Hu, C. Xue, D. Li, X. Zhu and T. Wu, 0D/1D heterostructure for efficient electrocatalytic $CO_2$-to-C1 conversion by ultra-small cluster-based multi-metallic sulfide nanoparticles and MWCNTs, *Chem. Eng. J.*, 2021, **422**, 130045.

24 X.-L. Wang, Z. Wu, X. Wang, C. Xue, C. Liu, J. Zhang, R. Zhou, D.-S. Li and T. Wu, Bifunctional electrocatalysts derived from cluster-based ternary sulfides for oxygen electrode reactions, *Electrochim. Acta*, 2021, **376**, 138048.

25 X. L. Wang, C. Xue, N. Kong, Z. Wu, J. Zhang, X. Wang, R. Zhou, H. Lin, Y. Li, D. S. Li and T. Wu, Molecular modulation of a molybdenum-selenium cluster by sulfur substitution to enhance the hydrogen evolution reaction, *Inorg. Chem.*, 2019, **58**, 12415–12421.

26 J. Zhang, C. Qin, Y. Zhong, X. Wang, W. Wang, D. Hu, X. Liu, C. Xue, R. Zhou, L. Shen, Y. Song, D. Xu, Z. Lin, J. Guo, H. Su, D.-S. Li and T. Wu, Atomically precise metal-chalcogenide semiconductor molecular nanoclusters with high dispersibility: Designed synthesis and intracluster photocarrier dynamics, *Nano Res.*, 2020, **13**, 2828–2836.

27 B. Peters, S. Santner, C. Donsbach, P. Vopel, B. Smarsly and S. Dehnen, Ionic liquid cations as methylation agent for extremely weak chalcogenido metalate nucleophiles, *Chem. Sci.*, 2019, **10**, 5211–5217.

28 B. Peters, G. Stuhrmann, F. Mack, F. Weigend and S. Dehnen, Highly soluble supertetrahedra upon selective partial butylation of chalcogenido metalate clusters in ionic liquids, *Angew. Chem., Int. Ed.*, 2021, **60**, 17622–17628.

29 T. Wu, X. Bu, P. Liao, L. Wang, S. T. Zheng, R. Ma and P. Feng, Superbase route to supertetrahedral chalcogenide clusters, *J. Am. Chem. Soc.*, 2012, **134**, 3619–3622.

30 Y. Wang, Z. Zhu, Z. Sun, Q. Hu, J. Li, J. Jiang and X. Huang, Discrete supertetrahedral T5 selenide clusters and their Se/S solid solutions: Ionic-liquid-assisted precursor route syntheses and photocatalytic properties, *Chem. – Eur. J.*, 2020, **26**, 1624–1632.

31 N.-N. Shen, B. Hu, C.-C. Cheng, G.-D. Zou, Q.-Q. Hu, C.-F. Du, J.-R. Li and X.-Y. Huang, Discrete supertetrahedral T3 InQ clusters (Q = S, S/Se, Se, Se/Te): Ionothermal syntheses and tunable optical and photodegradation properties, *Cryst. Growth Des.*, 2018, **18**, 962–968.

32 J. Wu, P. Sun, X. Wang, N. Chen and T. Wu, Ligand-partially-protected metal-chalcogenide supertetrahedral clusters, *Dalton Trans.*, 2022, **51**, 18257–18263.

33 F. Shahzad, M. Alhabeb, C. Hatter, B. Anasori, S. M. Hong, C. M. Koo and Y. Gogotsi, Electromagnetic interference shielding with 2D transition metal carbides (MXenes), *Science*, 2016, **353**, 1137–1140.

34 Y. Gao, C. Yan, H. Huang, T. Yang, G. Tian, D. Xiong, N. Chen, X. Chu, S. Zhong, W. Deng, Y. Fang and W. Yang,

 

Microchannel-confined MXene based flexible piezoresistive multifunctional micro-force sensor, *Adv. Funct. Mater.*, 2020, **30**, 1909603.

35 C. Peng, P. Wei, X. Li, Y. Liu, Y. Cao, H. Wang, H. Yu, F. Peng, L. Zhang, B. Zhang and K. Lv, High efficiency photocatalytic hydrogen production over ternary Cu/$TiO_2$@$Ti_3C_2T_x$ enabled by low-work-function 2D titanium carbide, *Nano Energy*, 2018, **53**, 97–107.

36 G. Zuo, Y. Wang, W. L. Teo, A. Xie, Y. Guo, Y. Dai, W. Zhou, D. Jana, Q. Xian, W. Dong and Y. Zhao, Ultrathin $ZnIn_2S_4$ nanosheets anchored on $Ti_3C_2T_x$ MXene for photocatalytic $H_2$ evolution, *Angew. Chem., Int. Ed.*, 2020, **59**, 11287–11292.

37 X. Xie, N. Zhang, Z.-R. Tang, M. Anpo and Y.-J. Xu, $Ti_3C_2T_x$ MXene as a Janus cocatalyst for concurrent promoted photoactivity and inhibited photocorrosion, *Appl. Catal., B*, 2018, **237**, 43–49.

38 Z. Wu, C. Li, Z. Li, K. Feng, M. Cai, D. Zhang, S. Wang, M. Chu, C. Zhang, J. Shen, Z. Huang, Y. Xiao, G. A. Ozin, X. Zhang and L. He, Niobium and titanium carbides (MXenes) as superior photothermal supports for $CO_2$ Photocatalysis, *ACS Nano*, 2021, **15**, 5696–5705.

39 M. Naguib, O. Mashtalir, J. Carle, V. Presser, J. Lu, L. Hultman, Y. Gogotsi and M. W. Barsoum, Two-dimensional transition metal carbides, *ACS Nano*, 2012, **6**, 1322–1331.

40 H. Wang, Y. Wu, X. Yuan, G. Zeng, J. Zhou, X. Wang and J. W. Chew, Clay-inspired MXene-based electrochemical devices and photo-electrocatalyst: State-of-the-art progresses and challenges, *Adv. Mater.*, 2018, **30**, e1704561.

41 Y. Ying, Y. Liu, X. Wang, Y. Mao, W. Cao, P. Hu and X. Peng, Two-dimensional titanium carbide for efficiently reductive removal of highly toxic chromium(VI) from water, *ACS Appl. Mater. Interfaces*, 2015, **7**, 1795–1803.

42 X. Sheng, Y. Zhao, L. Zhang and X. Lu, Properties of two-dimensional $Ti_3C_2$ MXene/thermoplastic polyurethane nanocomposites with effective reinforcement via melt blending, *Compos. Sci. Technol.*, 2019, **181**, 107710.

43 P. Lin, J. Xie, Y. He, X. Lu, W. Li, J. Fang, S. Yan, L. Zhang, X. Sheng and Y. Chen, MXene aerogel-based phase change materials toward solar energy conversion, *Sol. Energy Mater. Sol. Cells*, 2020, **206**, 110229.

44 J. Wu, B. Jin, X. Wang, Y. Ding, X.-L. Wang, D. Tang, X. Li, J. Shu, D.-S. Li, Q. Lin, Y.-B. Wu and T. Wu, Breakdown of valence shell electron pair repulsion theory in an H-bond-stabilized linear sp-hybridized sulfur, *CCS Chem.*, 2021, **3**, 2584–2590.

45 J. Ran, W. Guo, H. Wang, B. Zhu, J. Yu and S. Z. Qiao, Metal-free 2D/2D phosphorene/g-$C_3N_4$ van der Waals heterojunction for highly enhanced visible-light photocatalytic $H_2$ production, *Adv. Mater.*, 2018, **30**, e1800128.

46 J. Ran, G. Gao, F. T. Li, T. Y. Ma, A. Du and S. Z. Qiao, $Ti_3C_2$ MXene co-catalyst on metal sulfide photo-absorbers for enhanced visible-light photocatalytic hydrogen production, *Nat. Commun.*, 2017, **8**, 13907.

47 Z. Li, W. Huang, J. Liu, K. Lv and Q. Li, Embedding CdS@Au into Ultrathin $Ti_{3-x}C_2T_y$ to build dual Schottky barriers for photocatalytic $H_2$ production, *ACS Catal.*, 2021, **11**, 8510–8520.

48 L. Kavan, M. Gratzel, S. E. Gilbert, C. Klemenz and H. J. Scheel, Electrochemical and photoelectrochemical investigation of single-crystal anatase, *J. Am. Chem. Soc.*, 1996, **118**, 6716–6723.

49 P. Xia, S. Cao, B. Zhu, M. Liu, M. Shi, J. Yu and Y. Zhang, Designing a 0D/2D S-scheme heterojunction over polymeric carbon nitride for visible-light photocatalytic inactivation of bacteria, *Angew. Chem., Int. Ed.*, 2020, **59**, 5218–5225.

50 Z. Lin, J. Xiao, L. Li, P. Liu, C. Wang and G. Yang, Nanodiamond-embedded p-type copper(I) oxide nanocrystals for broad-spectrum photocatalytic hydrogen evolution, *Adv. Energy Mater.*, 2016, **6**, 1501865.

51 Z. Hu, G. Liu, X. Chen, Z. Shen and J. C. Yu, Enhancing charge separation in metallic photocatalysts: A case study of the conducting molybdenum dioxide, *Adv. Funct. Mater.*, 2016, **26**, 4445–4455.

52 F.-Y. Tian, D. Hou, F. Tang, M. Deng, X.-q. Qiao, Q. Zhang, T. Wu and D.-S. Li, Novel $Zn_{0.8}Cd_{0.2}S$@g-$C_3N_4$ core–shell heterojunctions with a twin structure for enhanced visible-light-driven photocatalytic hydrogen generation, *J. Mater. Chem. A*, 2018, **6**, 17086–17094.

53 M. Jakob, H. Levanon and P. V. Kamat, Charge distribution between UV-irradiated $TiO_2$ and gold nanoparticles: Determination of shift in the Fermi level, *Nano Lett.*, 2003, **3**, 353–358.

54 H. Yan, J. Yang, G. Ma, G. Wu, X. Zong, Z. Lei, J. Shi and C. Li, Visible-light-driven hydrogen production with extremely high quantum efficiency on Pt-PdS/CdS photocatalyst, *J. Catal.*, 2009, **266**, 165–168.

55 D. Y. Leung, X. Fu, C. Wang, M. Ni, M. K. Leung, X. Wang and X. Fu, Hydrogen production over titania-based photocatalysts, *ChemSusChem*, 2010, **3**, 681–694.

56 J. Yang, D. Wang, H. Han and C. Li, Roles of cocatalysts in photocatalysis and photoelectrocatalysis, *Acc. Chem. Res.*, 2013, **46**, 1900–1909.